Journal of Computational Physics 229 (2010) 7191–7206

Contents lists available at ScienceDirect

Journal of Computational Physics

journal homepage: www.elsevier.com/locate/jcp

A cell-centered Lagrangian scheme with the preservation of symmetry and conservation properties for compressible fluid flows in two-dimensional cylindrical geometry

Juan Cheng [a,1], Chi-Wang Shu [b,*,2]

[a] Institute of Applied Physics and Computational Mathematics, Beijing 100088, China
[b] Division of Applied Mathematics, Brown University, Providence, RI 02912, United States

ARTICLE INFO

Article history:
Received 9 February 2010
Received in revised form 24 April 2010
Accepted 4 June 2010
Available online 17 June 2010

Keywords:
Lagrangian scheme
Symmetry preservation
Conservative
Cell-centered
Compressible flow
Cylindrical coordinates

ABSTRACT

We develop a new cell-centered control volume Lagrangian scheme for solving Euler equations of compressible gas dynamics in cylindrical coordinates. The scheme is designed to be able to preserve one-dimensional spherical symmetry in a two-dimensional cylindrical geometry when computed on an equal-angle-zoned initial grid. Unlike many previous area-weighted schemes that possess the spherical symmetry property, our scheme is discretized on the true volume and it can preserve the conservation property for all the conserved variables including density, momentum and total energy. Several two-dimensional numerical examples in cylindrical coordinates are presented to demonstrate the performance of the scheme in terms of symmetry, accuracy and non-oscillatory properties.

1. Introduction

In numerical simulations of multidimensional fluid flow, there are two typical choices: a Lagrangian framework, in which the mesh moves with the local fluid velocity, and an Eulerian framework, in which the fluid flows through a grid fixed in space. More generally, the motion of the grid can also be chosen arbitrarily, resulting in the so-called Arbitrary Lagrangian–Eulerian method (ALE; see, e.g. [13]).

Both the Eulerian and Lagrangian methods have their own advantages and disadvantages. For example, the Eulerian method is easy to design arbitrarily high order schemes on the fixed grid so that it can simulate the smooth structure with high resolution and capture the discontinuity sharply without oscillations. Comparing with the Lagrangian method, it also has the advantage of being free from any trouble caused by grid distortion. Its main disadvantage lies in that it is relatively difficult to treat multi-material problems. Comparing with the Eulerian method, the Lagrangian method can reduce the numerical error which arises from the advection terms in the conservation equations and can capture material interfaces sharply and automatically. Due to the grid movement with the fluid, the Lagrangian method may encounter grid distortion

* Corresponding author. Tel.: +1 401 863 2549; fax: +1 401 863 1355.
E-mail addresses: cheng_juan@iapcm.ac.cn (J. Cheng), shu@dam.brown.edu (C.-W. Shu).

[1] Research is supported in part by NSFC Grants 10931004 and 10972043. Additional support is provided by the National Basic Research Program of China under Grant 2005CB321702.
[2] Research is supported in part by ARO Grant W911NF-08-1-0520 and NSF grant DMS-0809086.

0021-9991/$ - see front matter © 2010 Elsevier Inc. All rights reserved.
doi:10.1016/j.jcp.2010.06.007

problems, which could be solved by using the ALE approach, that is, when the grid is distorted, we rezone the grid to the optimal position and remap the variables from the old grid to the new grid.

Due to the distinguished advantage in capturing material interfaces sharply and automatically, the Lagrangian method is widely used in many fields for multi-material flow simulations such as astrophysics and inertial confinement fusion (ICF). In the past years, many efforts have been made to develop Lagrangian methods. Some algorithms are built on a staggered discretization in which velocity (momentum) is stored at vertices, while density and internal energy are stored at cell centers. The density/internal energy and velocity are solved on two different control volumes, see, e.g. [20,1,4]. The dissipation of kinetic energy into internal energy through shock waves is ensured by an artificial viscosity term [20,6,7]. Other algorithms start from the cell-centered discretization in which density, momentum and energy are all centered within cells and evolved on the same control volume. Advantages for the cell-centered schemes such as [11,19,8,9,16] include that this kind of methods is easy to remap when necessary and it does not require the addition of an explicit artificial viscosity for shock capturing. Numerical viscosity contained in the exact or approximate Riemann solver is usually enough to stabilize the algorithm.

In a Lagrangian simulation, it is a critical issue for a scheme to preserve certain symmetry (for example, cylindrical or spherical) in a coordinate system distinct from that symmetry. The importance of preserving physical symmetries in numerical simulation is well realized. As in the simulation of implosion problem with strong compressions, the preservation of spherical symmetry is significantly important, since the small deviation from spherical symmetry due to numerical errors may be exaggerated by Rayleigh–Taylor or some other instabilities which may potentially produce unpredictably large errors. On the other hand, to understand and predict the dynamics of implosion well, it is essential for us to know whether the asymmetric numerical result is due to the discrete error or to the physical intrinsic behavior.

Concerning the issue related to spherical symmetry preservation in two-dimensional cylindrical coordinates many works have been done mostly in the framework of staggered-grid hydrodynamics. The most widely used method that maintains spherical symmetry exactly on an equal-angle-zoned grid in cylindrical coordinates is the area-weighted method [26,2,22,25,4,17]. In this approach one uses a Cartesian form of the momentum equation in the cylindrical coordinate system, hence integration is performed on area rather than on the true volume in cylindrical coordinates. However, these area-weighted schemes might violate strict momentum and total energy conservation. This shortcoming of the schemes has been partially corrected in [4] by constructing a compatible area-weighted scheme which can preserve the conservation of total energy. However it seems that their flaw in the loss of momentum conservation has not been solved so far. Differently from the area-weighted scheme, Browne [3] presented a Lagrangian scheme termed "integrated total average" which is discretized on the true control volume in cylindrical coordinates. The scheme has been proven to be able to preserve the desired spherical symmetry in the two-dimensional cylindrical geometry for equal-angle zoning. Unfortunately, this scheme can not keep the momentum and total energy conservation and has the potential trouble in that if the initial mass in neighboring cells has a big difference, large error in acceleration may happen. Margolin and Shashkov use a curvilinear grid to construct symmetry-preserving discretizations for Lagrangian gas dynamics [18]. They use high-order curves to connect the nodes, so that planar, cylindrical and spherical symmetry are exactly preserved even on unequal-angle-zoned grids. In [5], Caramana and Whalen study the way to achieve the one-dimensional symmetry, in a two-dimensional coordinate system distinct from that symmetry by a simple modification of the gradient operator used to compute the force in a staggered-grid Lagrangian hydrodynamics algorithm.

In this paper, we propose a new cell-centered Lagrangian scheme on quadrilateral grids for solving compressible Euler equations in cylindrical coordinates. The scheme is based on a genuine volume discretization formulation. It preserves the conservation of mass, momentum and total energy. It is also designed to be able to preserve one-dimensional spherical symmetry in the two-dimensional cylindrical geometry for equal-angle-zoned initial grids.

An outline of the rest of this paper is as follows. In Section 2, we describe the individual steps of the Lagrangian scheme with the symmetry and conservation properties for Euler equations in cylindrical coordinates. In Section 3, numerical examples are given to demonstrate the performance of the new Lagrangian method. In Section 4 we will give concluding remarks.

2. A cell-centered conservative Lagrangian scheme with the preservation of spherical symmetry in cylindrical coordinates

2.1. The compressible Euler equations in a Lagrangian formulation in cylindrical coordinates

The compressible inviscid flow is governed by the Euler equations which have the following integral form in the Lagrangian formulation

$$\begin{cases} \frac{d}{dt}\iint_{\Omega(t)}\rho\, dV = 0, \\ \frac{d}{dt}\iint_{\Omega(t)}\mathbf{M}\, dV = -\int_{\Gamma(t)} p\mathbf{n}\, ds, \\ \frac{d}{dt}\iint_{\Omega(t)}E\, dV = -\int_{\Gamma(t)} p\mathbf{u}\cdot\mathbf{n}\, ds, \end{cases} \tag{2.1}$$

where ρ is the density, p is the pressure, $\mathbf{M}$ and $\mathbf{u}$ are the vectors of momentum and velocity respectively, and E is the total energy. $\mathbf{n}$ is the unit outward normal to the boundary $\Gamma(t)$.

In this paper, we seek to study the axisymmetric compressible Euler system. Its specific form in the cylindrical coordinates is as follows

$$\begin{cases} \frac{d}{dt}\iint_{\Omega(t)} \rho r\,dr\,dz = 0, \\ \frac{d}{dt}\iint_{\Omega(t)} M_z r\,dr\,dz = -\int_{\Gamma(t)} p n_z r\,dl, \\ \frac{d}{dt}\iint_{\Omega(t)} M_r r\,dr\,dz = -\int_{\Gamma(t)} p n_r r\,dl + \iint_{\Omega(t)} p\,dr\,dz, \\ \frac{d}{dt}\iint_{\Omega(t)} E r\,dr\,dz = -\int_{\Gamma(t)} p u_v r\,dl, \end{cases} \tag{2.2}$$

where z and r are the axial and radial directions respectively. $\mathbf{M} = (M_z, M_r)$, $\mathbf{u} = (u_z, u_r)$, where M_z, u_z, M_r, u_r are the momentum and velocity components in the z and r directions respectively, $\mathbf{n} = (n_z, n_r)$ is the unit outward normal to the boundary $\Gamma(t)$ in the $z-r$ coordinates, and $u_v = (u_z, u_r)\cdot\mathbf{n}$ is the normal velocity at $\Gamma(t)$.

The set of equations is completed by the addition of an equation of state (EOS) with the following general form

$$p = p(\rho, e), \tag{2.3}$$

where $e = \frac{E}{\rho} - \frac{1}{2}|\mathbf{u}|^2$ is the specific internal energy. Especially, if we consider the ideal gas, then the equation of state has a simpler form,

$$p = (\gamma - 1)\rho e,$$

where γ is a constant representing the ratio of specific heat capacities of the fluid.

2.2. The construction of the scheme

Fig. 2.1 indicates the cylindrical geometry (z, r) we are concerned with. The 2D spatial domain Ω is discretized into $K \times L$ computational cells. Fig. 2.1 shows an equal-angle-zoned grids with logical l-lines radially outward and logical k-lines in the angular direction. $I_{k+\frac{1}{2},l+\frac{1}{2}}$ is a quadrilateral cell constructed by the four vertices $\{(z_{k,l}, r_{k,l}), (z_{k+1,l}, r_{k+1,l}), (z_{k+1,l+1}, r_{k+1,l+1}), (z_{k,l+1}, r_{k,l+1})\}$. $S_{k+\frac{1}{2},l+\frac{1}{2}}$ and $V_{k+\frac{1}{2},l+\frac{1}{2}}$ denote the area and volume of the cell $I_{k+\frac{1}{2},l+\frac{1}{2}}$ with $k = 1,\ldots,K$, $l = 1,\ldots,L$ respectively, where the volume of the cell refers to that of the circular ring obtained by rotating this cell around the z-axis. Here for simplicity and without any confusion, the volume of the cell is considered as that of the circular ring on unit arc in the azimuthal direction, namely we omit the factor 2π which should appear in the integration of the real volume. The fluid velocity $((u_z)_{k,l}, (u_r)_{k,l})$ is defined at the vertex of grid.

In this paper, in order to obtain a scheme with both the spherical symmetry and conservation properties in a 2D cylindrical geometry, we will discretize the momentum equation in (2.2) along the local polar and angular directions (ξ, θ) rather than in the usual z and r directions in each cell, where ξ is the radial direction passing through the cell center and the origin. For an equal-angle-zoned grid, the cell shown in Fig. 2.1 is an equal-sided trapezoid, it has the property that the angles between ξ and the two equal sides of the cell are the same. θ is the angular direction which is orthogonal to ξ, see Fig. 2.1. After completing the momentum discretization, we transform them back to the original cylindrical (z, r) coordinates. This is similar in spirit to the local characteristic decomposition procedure in limiting, where the relevant quantities are first transformed to the local characteristic fields, then the limiting procedure is performed, and afterwards the result is transformed back to the original component space. In the actual implementation, once the local ξ and θ directions for each cell are determined at the initial time, these directions will not change for later time. To perform this local coordinate transformation, in each cell, the Euler equations in cylindrical coordinates are rewritten in the following form

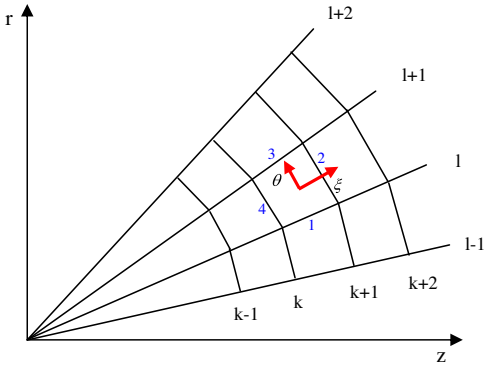

Fig. 2.1. Equi-angular polar grid for cylindrical geometry.

$$\begin{cases} \frac{d}{dt}\iint_{I_{k+\frac{1}{2},l+\frac{1}{2}}} \rho r\,dr\,dz = 0, \\ \frac{d}{dt}\iint_{I_{k+\frac{1}{2},l+\frac{1}{2}}} M_\xi r\,dr\,dz = -\int_{\partial I_{k+\frac{1}{2},l+\frac{1}{2}}} p n_\xi r\,dl + \iint_{I_{k+\frac{1}{2},l+\frac{1}{2}}} p\sin\varphi\,dr\,dz, \\ \frac{d}{dt}\iint_{I_{k+\frac{1}{2},l+\frac{1}{2}}} M_\theta r\,dr\,dz = -\int_{\partial I_{k+\frac{1}{2},l+\frac{1}{2}}} p n_\theta r\,dl + \iint_{I_{k+\frac{1}{2},l+\frac{1}{2}}} p\cos\varphi\,dr\,dz, \\ \frac{d}{dt}\iint_{I_{k+\frac{1}{2},l+\frac{1}{2}}} E r\,dr\,dz = -\int_{\partial I_{k+\frac{1}{2},l+\frac{1}{2}}} p u_v r\,dl, \end{cases} \tag{2.4}$$

where M_ξ and M_θ are the component values of momentum in the local ξ and θ directions respectively, $\mathbf{n} = (n_\xi, n_\theta)$ is the unit outward normal of the cell boundary $\partial I_{i+\frac{1}{2},j+\frac{1}{2}}$, and φ is the angle between the radial direction passing through the corresponding point and the axial coordinate z. The value of ξ is denoted as the radial radius which represents the distance to the origin. Thus we have $z = \xi\cos\varphi$, $r = \xi\sin\varphi$ and $\xi = \sqrt{z^2 + r^2}$.

For the cell-centered scheme, all the variables except velocity are stored at the cell center of $I_{k+\frac{1}{2},l+\frac{1}{2}}$ in the form of cell averages. For example, the values of the cell averages for the cell $I_{k+\frac{1}{2},l+\frac{1}{2}}$, denoted by $\bar{\rho}_{k+\frac{1}{2},l+\frac{1}{2}}$, $\overline{M}^{\xi}_{k+\frac{1}{2},l+\frac{1}{2}}$, $\overline{M}^{\theta}_{k+\frac{1}{2},l+\frac{1}{2}}$ and $\overline{E}_{k+\frac{1}{2},l+\frac{1}{2}}$, are defined as follows

$$\begin{aligned} \bar{\rho}_{k+\frac{1}{2},l+\frac{1}{2}} &= \frac{1}{V_{k+\frac{1}{2},l+\frac{1}{2}}}\iint_{I_{k+\frac{1}{2},l+\frac{1}{2}}} \rho r\,dr\,dz, \\ \overline{M}^{\xi}_{k+\frac{1}{2},l+\frac{1}{2}} &= \frac{1}{V_{k+\frac{1}{2},l+\frac{1}{2}}}\iint_{I_{k+\frac{1}{2},l+\frac{1}{2}}} M_\xi r\,dr\,dz, \\ \overline{M}^{\theta}_{k+\frac{1}{2},l+\frac{1}{2}} &= \frac{1}{V_{k+\frac{1}{2},l+\frac{1}{2}}}\iint_{I_{k+\frac{1}{2},l+\frac{1}{2}}} M_\theta r\,dr\,dz, \\ \overline{E}_{k+\frac{1}{2},l+\frac{1}{2}} &= \frac{1}{V_{k+\frac{1}{2},l+\frac{1}{2}}}\iint_{I_{k+\frac{1}{2},l+\frac{1}{2}}} E r\,dr\,dz, \end{aligned}$$

where $V_{k+\frac{1}{2},l+\frac{1}{2}} = \iint_{I_{k+\frac{1}{2},l+\frac{1}{2}}} r\,dr\,dz$. In our scheme, the cell averages of the above conserved variables are evolved in time, as a regular finite volume scheme.

2.2.1. Spatial discretization

We first formulate the semi-discrete finite volume scheme of the governing equations (2.4) as

$$\frac{d}{dt}\begin{pmatrix} \bar{\rho}_{k+\frac{1}{2},l+\frac{1}{2}} V_{k+\frac{1}{2},l+\frac{1}{2}} \\ \overline{M^\xi}_{k+\frac{1}{2},l+\frac{1}{2}} V_{k+\frac{1}{2},l+\frac{1}{2}} \\ \overline{M^\theta}_{k+\frac{1}{2},l+\frac{1}{2}} V_{k+\frac{1}{2},l+\frac{1}{2}} \\ \overline{E}_{k+\frac{1}{2},l+\frac{1}{2}} V_{k+\frac{1}{2},l+\frac{1}{2}} \end{pmatrix} = -\int_{\partial I_{k+\frac{1}{2},l+\frac{1}{2}}} \widehat{\mathbf{F}}\,dl + \begin{pmatrix} 0 \\ (p_c)_{k+\frac{1}{2},l+\frac{1}{2}}\sin(\varphi_c)_{k+\frac{1}{2},l+\frac{1}{2}} s_{k+\frac{1}{2},l+\frac{1}{2}} \\ (p_c)_{k+\frac{1}{2},l+\frac{1}{2}}\cos(\varphi_c)_{k+\frac{1}{2},l+\frac{1}{2}} s_{k+\frac{1}{2},l+\frac{1}{2}} \\ 0 \end{pmatrix}, \tag{2.5}$$

where

$$\int_{\partial I_{k+\frac{1}{2},l+\frac{1}{2}}} \widehat{\mathbf{F}}\,dl = \int_{\partial I_{k+\frac{1}{2},l+\frac{1}{2}}} \begin{pmatrix} \hat{f}_D(\mathbf{U}_v^-, \mathbf{U}_v^+) \\ \hat{f}_{M^\xi}(\mathbf{U}_v^-, \mathbf{U}_v^+) \\ \hat{f}_{M^\theta}(\mathbf{U}_v^-, \mathbf{U}_v^+) \\ \hat{f}_E(\mathbf{U}_v^-, \mathbf{U}_v^+) \end{pmatrix} dl \tag{2.6}$$

and

$$\begin{cases} \hat{f}_D(\mathbf{U}_v, \mathbf{U}_v) = 0, \\ \hat{f}_{M^\xi}(\mathbf{U}_v, \mathbf{U}_v) = p n_\xi r, \\ \hat{f}_{M^\theta}(\mathbf{U}_v, \mathbf{U}_v) = p n_\theta r, \\ \hat{f}_E(\mathbf{U}_v, \mathbf{U}_v) = p u_v r, \end{cases} \tag{2.7}$$

$\hat{f}_D$, $\hat{f}_{M^\xi}$, $\hat{f}_{M^\theta}$ and $\hat{f}_E$ are the numerical fluxes for mass, ξ-momentum, θ-momentum and total energy across the cell boundary respectively. $\mathbf{U}_v^\pm = (\rho^\pm, M_v^\pm, E^\pm)$ are the values of density, normal component of momentum and total energy at both sides of the cell boundary, where $M_v^\pm = (M_\xi^\pm, M_\theta^\pm)\cdot\mathbf{n}$. $(p_c)_{k+\frac{1}{2},l+\frac{1}{2}}$ is the pressure at the cell center. $(\varphi_c)_{k+\frac{1}{2},l+\frac{1}{2}}$ is set to be the angle between the local ξ direction and the z coordinate.

The first step for establishing the scheme is to determine the line integral term on the right side of Eq. (2.5). Suppose the cell boundary $\partial I_{k+\frac{1}{2},l+\frac{1}{2}}$ consists of M edges. The line integral concerned with the flux in Eq. (2.5) is discretized by the following formula

$$\int_{\partial I_{k+\frac{1}{2},l+\frac{1}{2}}} \widehat{\mathbf{F}}\, dl \approx \sum_{m=1}^{M} \widehat{\mathbf{F}}(\mathbf{U}_v^{m+}, \mathbf{U}_v^{m-})\Delta l^m, \tag{2.8}$$

where Δl^m is the length of the cell edge m. $\widehat{\mathbf{F}}(\mathbf{U}_v^{m+}, \mathbf{U}_v^{m-})$ is a numerical flux at the edge m.

To determine the fluxes $\widehat{\mathbf{F}} = (\hat{f}_D, \hat{f}_{M^\xi}, \hat{f}_{M^\theta}, \hat{f}_E)$ at the edges of the quadrilateral shaped cell, we first need to identify the values of the primitive variables at each side of the edge, that is $\mathbf{U}_v^{m\pm}$, $m = 1,4$. Here we use the information of the left and right cell average values of the conserved variables. We define the direction of each edge of the cell to be the increasing direction of the index k or l, for example the direction of the edge with two endpoints (k,l) and $(k+1,l)$ is from (k,l) to $(k+1,l)$. Thus, for example, for Edge 1 in the cell $I_{k+\frac{1}{2},l+\frac{1}{2}}$ in Fig. 2.1, we obtain $\mathbf{U}_v^{1-} = (\rho_{k+\frac{1}{2},l+\frac{1}{2}}, (M_v)_{k+\frac{1}{2},l+\frac{1}{2}}, E_{k+\frac{1}{2},l+\frac{1}{2}})$ and $\mathbf{U}_v^{1+} = (\rho_{k+\frac{1}{2},l-\frac{1}{2}}, (M_v)_{k+\frac{1}{2},l-\frac{1}{2}}, E_{k+\frac{1}{2},l-\frac{1}{2}})$ at the two sides of Edge 1.

Next, we will compute the fluxes given the primitive states $\{\mathbf{U}_v^{m\pm},\ m = 1,4\}$ at each side of the cell boundary. Here as an example, we use the Dukowicz numerical flux [12] to obtain the fluxes at the cell boundary by the following procedure. Other numerical fluxes such as the Godunov or acoustic fluxes obtained from exact or approximate Riemann solvers can also be used and the proof of the symmetry preservation property will go through as well. We have also tested our scheme on a few other numerical fluxes such as the Godunov flux and the acoustic flux. The results show that these two fluxes can work as well as the Dukowicz flux. For a more in-depth discussion on the differences in the features and numerical performance between different numerical fluxes, we refer to our previous paper [8].

The velocity u_v^m at Edge m is obtained by solving the following semi-quadratic equation,

$$\rho^{m+}A^{m+}\left|u_v^m - u_{\min}^{m*}\right|\left(u_v^m - u_{\min}^{m*}\right) + \rho^{m-}A^{m-}\left|u_v^m - u_{\max}^{m*}\right|\left(u_v^m - u_{\max}^{m*}\right) + p^{m+,*} - p^{m-,*} = 0, \tag{2.9}$$

where

$$\begin{aligned} &u_{\min}^{m*} = u_v^{m+} - c^{m+}/2A^{m+}, \quad u_{\max}^{m*} = u_v^{m-} + c^{m-}/2A^{m-};\\ &p^{m+,*} = p^{m+} - \frac{1}{4}\rho^{m+}(c^{m+})^2/A^{m+}, \quad p^{m-,*} = p^{m-} - \frac{1}{4}\rho^{m-}(c^{m-})^2/A^{m-}. \end{aligned} \tag{2.10}$$

Here $\rho^{m\pm}$, $u_v^{m\pm}$, $p^{m\pm}$ are the left and right values of density, velocity and pressure at Edge m respectively, $c^\pm$ are the left and right values of the sound speed at Edge m and $A^\pm$ are parameters directly related to the shock density ratio in the limit of strong shocks. We refer to [12] for the details of the definition of $A^\pm$. In particular, for an ideal gas, $A^\pm = (\gamma+1)/2$.

After we have calculated the velocity u_v^m, the pressure p^m at Edge m is easily obtained by the following equation

$$p^m = \frac{1}{2}(p^{m-,*} + p^{m+,*}) + \frac{1}{2}\rho^{m+}A^{m+}\left|u_v^m - u_{\min}^{m*}\right|\left(u_v^m - u_{\min}^{m*}\right) - \frac{1}{2}\rho^{m-}A^{m-}\left|u_v^m - u_{\max}^{m*}\right|\left(u_v^m - u_{\max}^{m*}\right). \tag{2.11}$$

If p^m is found to be negative which predicts cavitation, then we set $p^m = 0$.

Thus we can get the fluxes $\hat{f}_D$, $\hat{f}_{M^\xi}$, $\hat{f}_{M^\theta}$ and $\hat{f}_E$ at Edge m as follows

$$\begin{cases} \hat{f}_D(\mathbf{U}_v^{m-}, \mathbf{U}_v^{m+}) = 0,\\ \hat{f}_{M^\xi}(\mathbf{U}_v^{m-}, \mathbf{U}_v^{m+}) = p^m n_\xi^m r_e^m,\\ \hat{f}_{M^\theta}(\mathbf{U}_v^{m-}, \mathbf{U}_v^{m+}) = p^m n_\theta^m r_e^m,\\ \hat{f}_E(\mathbf{U}_v^{m-}, \mathbf{U}_v^{m+}) = p^m u_v^m r_e^m, \end{cases} \tag{2.12}$$

where (n_ξ^m, n_θ^m) and r_e^m are the unit outward normal direction and the r coordinate of the middle point of Edge m respectively. We have now finished the determination of the flux term in Eq. (2.5).

As to the source term in Eq. (2.5), the way to determine $(p_c)_{k+\frac{1}{2},l+\frac{1}{2}}$ is the key for obtaining the control volume scheme with the spherical symmetry property. Here $(p_c)_{k+\frac{1}{2},l+\frac{1}{2}}$ is denoted as

$$(p_c)_{k+\frac{1}{2},l+\frac{1}{2}} = \frac{1}{2}(p^1 + p^3), \tag{2.13}$$

where p^1 and p^3 are the values of pressure at Edges 1 and 3 of Cell $I_{k+\frac{1}{2},l+\frac{1}{2}}$ (see Fig. 2.1) obtained in the above flux determination procedure. Based on the above manipulation, the scheme can preserve the conservation for all the conserved variables, since it is discretized on the true volume and the numerical flux across each cell boundary is single-valued for the update of its two neighboring cells. Meanwhile, we can also prove that the scheme can keep the spherical symmetry property if equi-angular polar initial grids are used. The proof will be given in the last subsection of this section.

2.2.2. The determination of the vertex velocity

The vertex velocity of the mesh is determined in the same way as in [8]. Briefly, we first obtain the tangential and normal velocities along each edge, specifically, the tangential velocity of the vertex (or edge center) along the edge is defined as a simple average of that in both sides. The normal velocity is obtained by the value of velocity through the Dukowicz approximate Riemann solver along the normal direction of the edge. Then the velocity of the vertex is set to be the arithmetic average of the velocities along the edges which share this vertex.

2.2.3. Time discretization

The time marching for the semi-discrete scheme (2.5) can be accomplished by the Euler forward method. Thus the fully discretized scheme can be written as follows

$$\begin{pmatrix} \bar{\rho}^{n+1}_{k+\frac{1}{2},l+\frac{1}{2}} V^{n+1}_{k+\frac{1}{2},l+\frac{1}{2}} - \bar{\rho}^{n}_{k+\frac{1}{2},l+\frac{1}{2}} V^{n}_{k+\frac{1}{2},l+\frac{1}{2}} \\ \overline{M}^{\xi,n+1}_{k+\frac{1}{2},l+\frac{1}{2}} V^{n+1}_{k+\frac{1}{2},l+\frac{1}{2}} - \overline{M}^{\xi,n}_{k+\frac{1}{2},l+\frac{1}{2}} V^{n}_{k+\frac{1}{2},l+\frac{1}{2}} \\ \overline{M}^{\theta,n+1}_{k+\frac{1}{2},l+\frac{1}{2}} V^{n+1}_{k+\frac{1}{2},l+\frac{1}{2}} - \overline{M}^{\theta,n}_{k+\frac{1}{2},l+\frac{1}{2}} V^{n}_{k+\frac{1}{2},l+\frac{1}{2}} \\ \overline{E}^{n+1}_{k+\frac{1}{2},l+\frac{1}{2}} V^{n+1}_{k+\frac{1}{2},l+\frac{1}{2}} - \overline{E}^{n}_{k+\frac{1}{2},l+\frac{1}{2}} V^{n}_{k+\frac{1}{2},l+\frac{1}{2}} \end{pmatrix} = \Delta t^n \left(-\sum_{m=1}^{M} \widehat{\mathbf{F}}(\mathbf{U}^{m,n}_v)\Delta l^{m,n} + \begin{pmatrix} 0 \\ (p_c)^n_{k+\frac{1}{2},l+\frac{1}{2}} \sin(\varphi_c)^n_{k+\frac{1}{2},l+\frac{1}{2}} s^n_{k+\frac{1}{2},l+\frac{1}{2}} \\ (p_c)^n_{k+\frac{1}{2},l+\frac{1}{2}} \cos(\varphi_c)^n_{k+\frac{1}{2},l+\frac{1}{2}} s^n_{k+\frac{1}{2},l+\frac{1}{2}} \\ 0 \end{pmatrix} \right). \tag{2.14}$$

Here the variables with the superscripts 'n' and '$n+1$' represent the values of the corresponding variables at the nth and $(n+1)$th time steps respectively. The scheme (2.14) is consistent with the Euler equations (2.4) and has first order accuracy in space and time.

The time step Δt^n is chosen as follows

$$\Delta t^n = \lambda \min_{k=1,\ldots,K,l=1,\ldots,L} \left(\Delta l^n_{k+\frac{1}{2},l+\frac{1}{2}} / c^n_{k+\frac{1}{2},l+\frac{1}{2}} \right), \tag{2.15}$$

where $\Delta l^n_{k+\frac{1}{2},l+\frac{1}{2}}$ is the shortest edge length of the cell $I_{k+\frac{1}{2},l+\frac{1}{2}}$, and $c^n_{k+\frac{1}{2},l+\frac{1}{2}}$ is the sound speed within this cell. The Courant number λ in the following tests is set to be 0.5 unless otherwise stated.

In our numerical tests, the scheme in Eq. (2.14) can work well in most cases. However in some of the more demanding tests, the scheme is observed to show some instability. It seems that a good way to enhance stability is to use the second-order TVD Runge–Kutta method [24] for the time discretization. Then the scheme shows very satisfactory stability in all our numerical tests. We refer the reader to [8] for the implementation details on high order Runge–Kutta methods in a Lagrangian scheme. The usage of higher order TVD Runge–Kutta time discretization simply to enhance stability, not to increase the order of accuracy, can also be found in [27].

2.2.4. Proof of the spherical symmetry preservation property

In this section, we will prove our scheme (2.14) can keep the spherical symmetry property computed on an equal-angle-zoned initial grid. Due to the special structure of TVD Runge–Kutta methods [24], that they are convex combinations of Euler forward steps, the same symmetry-preserving property still holds if it is proved for the Euler forward time discretization.

Theorem. *The scheme (2.14) can keep the one-dimensional spherical symmetry property computed on an equal-angle-zoned initial grid. That is, if the solution has one-dimensional spherical symmetry at the initial time, then the computational solution will keep this symmetry with the time marching.*

Proof. Without loss of the generality, we only need to prove the solution of the scheme (2.14) can keep the spherical symmetry at $(n+1)$th step, if the solution is known to be of spherical symmetry at nth step. Notice that, for the Lagrangian solution, symmetry preserving refers to the evolution of both the conserved variables and the grids. □

For the convenience of notation, we adopt the convention that variables without the superscript '$n+1$' are those at the nth time step. Assume that at the nth step the grid is a polar grid with equal angles (see Fig. 2.1) and the cell averages of the conserved variables including density, momentum and total energy are symmetrical on this grid, namely these variables in the cells with the same k indices are identical. For simplicity, in the following we will omit the subscript '$l+\frac{1}{2}$' for the variables which are independent of the l index, for example,

$$\begin{cases} \bar{\rho}^n_{k+\frac{1}{2},l+\frac{1}{2}} = \bar{\rho}_{k+\frac{1}{2}}, \\ \overline{M}^{\xi,n}_{k+\frac{1}{2},l+\frac{1}{2}} = \overline{M}^{\xi}_{k+\frac{1}{2}}, \\ \overline{M}^{\theta,n}_{k+\frac{1}{2},l+\frac{1}{2}} = \overline{M}^{\theta}_{k+\frac{1}{2}} = 0, \\ \overline{E}^n_{k+\frac{1}{2},l+\frac{1}{2}} = \overline{E}_{k+\frac{1}{2}}, \\ s^n_{k+\frac{1}{2},l+\frac{1}{2}} = s_{k+\frac{1}{2}}, \quad \text{for } k = 1,\ldots K,\ l = 1,\ldots,L. \end{cases} \tag{2.16}$$

Next we denote some variables concerning the grid geometry. For simplicity, in the following text, we omit the subscript '$(k+\frac{1}{2}, l+\frac{1}{2})$' for the quantities corresponding to the cell edge if it will not bring any confusion. $\Delta\varphi$ denotes the angle between any two neighboring l lines which is a constant for the equi-angular polar grid under consideration. The value of ξ at the middle point of each edge is defined as $\xi^m_e,\ m = 1,4$, the length of each cell edge is denoted as $\{\Delta l^m, m = 1,4\}$. Since the grid is symmetrical, ξ^m_e and Δl^m, for $m = 1,4$, are independent of the l index, thus we denote them as

$$\begin{aligned} &\xi^1_e = \xi^3_e = \xi_{k+\frac{1}{2}}, \quad \xi^2_e = \xi_{k+1}, \quad \xi^4_e = \xi_k, \\ &\Delta l^1 = \Delta l^3 = \Delta l_{k+\frac{1}{2}}, \quad \Delta l^2 = \Delta l_{k+1}, \quad \Delta l^4 = \Delta l_k. \end{aligned} \tag{2.17}$$

Considering an arbitrary cell $I_{k+\frac{1}{2},l+\frac{1}{2}}$, for the convenience of proof, in the following, we will project all the variables relative to the determination of the cell's flux and velocity to its local ξ–θ coordinates. For example, the outward normal direction $\mathbf{n} = (n_\xi, n_\theta)$ of the cell's four edges in the local ξ–θ coordinates are as follows

$$\begin{aligned}
&(n_\xi^1, n_\theta^1) = \left(-\sin\left(\frac{1}{2}\Delta\varphi\right), -\cos\left(\frac{1}{2}\Delta\varphi\right)\right),\\
&(n_\xi^2, n_\theta^2) = (1, 0),\\
&(n_\xi^3, n_\theta^3) = \left(-\sin\left(\frac{1}{2}\Delta\varphi\right), \cos\left(\frac{1}{2}\Delta\varphi\right)\right),\\
&(n_\xi^4, n_\theta^4) = (-1, 0).
\end{aligned}$$

In the following, we will first prove the symmetry of the grid at the $(n+1)$th step.

We will look at the velocity on each cell edge first. For this purpose we need to determine $\mathbf{U}_v^{m\pm} = (\rho^{m\pm}, M_v^{m\pm}, E^{m\pm})$ and $M_t^{m\pm}$, for $m = 1,4$, where $M_t^{m\pm}$ is the tangential momentum at the two sides of Edge m. (ρ^m, M_v^m, E^m) denote density, normal momentum and total energy at the edge which are obtained from $\mathbf{U}_v^{m\pm}$ through the Dukowicz approximate Riemann solver. The pressure, normal velocity and tangential velocity at Edge m are defined as p^m, u_v^m, u_t^m respectively, where $u_t^m = \frac{1}{2}(M_t^{m-}/\rho^{m-} + M_t^{m+}/\rho^{m+})$, $u_v^m = M_v^m/\rho^m$.

Using (2.16), we have

$$\begin{aligned}
&\rho^{1\pm} = \bar{\rho}_{k+\frac{1}{2}},\\
&E^{1\pm} = \overline{E}_{k+\frac{1}{2}},\\
&\rho^{2-} = \bar{\rho}_{k+\frac{1}{2}}, \quad \rho^{2+} = \bar{\rho}_{k+\frac{3}{2}},\\
&E^{2-} = \overline{E}_{k+\frac{1}{2}}, \quad E^{2+} = \overline{E}_{k+\frac{3}{2}},\\
&\rho^{3\pm} = \bar{\rho}_{k+\frac{1}{2}},\\
&E^{3\pm} = \overline{E}_{k+\frac{1}{2}},\\
&\rho^{4-} = \bar{\rho}_{k-\frac{1}{2}}, \quad \rho^{4+} = \bar{\rho}_{k+\frac{1}{2}},\\
&E^{4-} = \overline{E}_{k-\frac{1}{2}}, \quad E^{4+} = \overline{E}_{k+\frac{1}{2}}.
\end{aligned}$$

As to the momentum involved in Eq. (2.14), by simple manipulation, we can obtain the momentum at four edges of Cell $I_{k+\frac{1}{2},l+\frac{1}{2}}$ in its local ξ–θ coordinates,

$$\begin{aligned}
&M_\xi^{1-} = \overline{M}_{k+\frac{1}{2}}^\xi, \quad M_\theta^{1-} = 0,\\
&M_\xi^{1+} = \overline{M}_{k+\frac{1}{2}}^\xi \cos(\Delta\varphi), \quad M_\theta^{1+} = -\overline{M}_{k+\frac{1}{2}}^\xi \sin(\Delta\varphi),\\
&M_\xi^{2-} = \overline{M}_{k+\frac{1}{2}}^\xi, \quad M_\theta^{2-} = 0,\\
&M_\xi^{2+} = \overline{M}_{k+\frac{3}{2}}^\xi, \quad M_\theta^{2+} = 0,\\
&M_\xi^{3-} = \overline{M}_{k+\frac{1}{2}}^\xi \cos(\Delta\varphi), \quad M_\theta^{3-} = \overline{M}_{k+\frac{1}{2}}^\xi \sin(\Delta\varphi),\\
&M_\xi^{3+} = \overline{M}_{k+\frac{1}{2}}^\xi, \quad M_\theta^{3+} = 0,\\
&M_\xi^{4-} = \overline{M}_{k-\frac{1}{2}}^\xi, \quad M_\theta^{4-} = 0,\\
&M_\xi^{4+} = \overline{M}_{k+\frac{1}{2}}^\xi, \quad M_\theta^{4+} = 0.
\end{aligned}$$

Thus,

$$\begin{aligned}
&M_v^{1-} = (M_\xi^{1-}, M_\theta^{1-}) \cdot (n_\xi^1, n_\theta^1) = -\sin\left(\frac{1}{2}\Delta\varphi\right)\overline{M}_{k+\frac{1}{2}}^\xi,\\
&M_v^{1+} = (M_\xi^{1+}, M_\theta^{1+}) \cdot (n_\xi^1, n_\theta^1) = \sin\left(\frac{1}{2}\Delta\varphi\right)\overline{M}_{k+\frac{1}{2}}^\xi,\\
&M_v^{2-} = \left(M_\xi^{2-}, M_\theta^{2-}\right) \cdot (n_\xi^2, n_\theta^2) = \overline{M}_{k+\frac{1}{2}}^\xi,\\
&M_v^{2+} = \left(M_\xi^{2+}, M_\theta^{2+}\right) \cdot (n_\xi^2, n_\theta^2) = \overline{M}_{k+\frac{3}{2}}^\xi,\\
&M_v^{3-} = \left(M_\xi^{3-}, M_\theta^{3-}\right) \cdot (n_\xi^3, n_\theta^3) = \sin\left(\frac{1}{2}\Delta\varphi\right)\overline{M}_{k+\frac{1}{2}}^\xi,\\
&M_v^{3+} = \left(M_\xi^{3+}, M_\theta^{3+}\right) \cdot (n_\xi^3, n_\theta^3) = -\sin\left(\frac{1}{2}\Delta\varphi\right)\overline{M}_{k+\frac{1}{2}}^\xi,
\end{aligned}$$

$$M_v^{4-} = \left(M_\xi^{4-}, M_\theta^{4-}\right)\cdot(n_\xi^4, n_\theta^4) = -\overline{M}^\xi_{k-\frac{1}{2}},$$
$$M_v^{4+} = \left(M_\xi^{4+}, M_\theta^{4+}\right)\cdot(n_\xi^4, n_\theta^4) = -\overline{M}^\xi_{k+\frac{1}{2}},$$

and

$$M_t^{1-} = \left(M_\xi^{1-}, M_\theta^{1-}\right)\cdot\left(\cos\left(\frac{1}{2}\Delta\varphi\right), -\sin\left(\frac{1}{2}\Delta\varphi\right)\right) = \cos\left(\frac{1}{2}\Delta\varphi\right)\overline{M}^\xi_{k+\frac{1}{2}},$$
$$M_t^{1+} = \left(M_\xi^{1+}, M_\theta^{1+}\right)\cdot\left(\cos\left(\frac{1}{2}\Delta\varphi\right), -\sin\left(\frac{1}{2}\Delta\varphi\right)\right) = \cos\left(\frac{1}{2}\Delta\varphi\right)\overline{M}^\xi_{k+\frac{1}{2}},$$
$$M_t^{2-} = M_t^{2+} = 0,$$
$$M_t^{3-} = (M_\xi^{3-}, M_\theta^{3-})\cdot\left(\cos\left(\frac{1}{2}\Delta\varphi\right), \sin\left(\frac{1}{2}\Delta\varphi\right)\right) = \cos\left(\frac{1}{2}\Delta\varphi\right)\overline{M}^\xi_{k+\frac{1}{2}},$$
$$M_t^{3+} = \left(M_\xi^{3+}, M_\theta^{3+}\right)\cdot\left(\cos\left(\frac{1}{2}\Delta\varphi\right), \sin\left(\frac{1}{2}\Delta\varphi\right)\right) = \cos\left(\frac{1}{2}\Delta\varphi\right)\overline{M}^\xi_{k+\frac{1}{2}},$$
$$M_t^{4-} = M_t^{4+} = 0.$$

Then we have

$$\mathbf{U}_v^{1-} = \left(\bar\rho_{k+\frac{1}{2}}, -\sin\left(\frac{1}{2}\Delta\varphi\right)\overline{M}^\xi_{k+\frac{1}{2}}, \overline{E}_{k+\frac{1}{2}}\right), \quad \mathbf{U}_v^{1+} = \left(\bar\rho_{k+\frac{1}{2}}, \sin\left(\frac{1}{2}\Delta\varphi\right)\overline{M}^\xi_{k+\frac{1}{2}}, \overline{E}_{k+\frac{1}{2}}\right),$$
$$\mathbf{U}_v^{3-} = \left(\bar\rho_{k+\frac{1}{2}}, \sin\left(\frac{1}{2}\Delta\varphi\right)\overline{M}^\xi_{k+\frac{1}{2}}, \overline{E}_{k+\frac{1}{2}}\right), \quad \mathbf{U}_v^{3+} = \left(\bar\rho_{k+\frac{1}{2}}, -\sin\left(\frac{1}{2}\Delta\varphi\right)\overline{M}^\xi_{k+\frac{1}{2}}, \overline{E}_{k+\frac{1}{2}}\right),$$
$$\mathbf{U}_v^{2-} = \left(\bar\rho_{k+\frac{1}{2}}, \overline{M}^\xi_{k+\frac{1}{2}}, \overline{E}_{k+\frac{1}{2}}\right), \quad \mathbf{U}_v^{2+} = \left(\bar\rho_{k+\frac{3}{2}}, \overline{M}^\xi_{k+\frac{3}{2}}, \overline{E}_{k+\frac{3}{2}}\right),$$
$$\mathbf{U}_v^{4-} = \left(\bar\rho_{k-\frac{1}{2}}, -\overline{M}^\xi_{k-\frac{1}{2}}, \overline{E}_{k-\frac{1}{2}}\right), \quad \mathbf{U}_v^{4+} = \left(\bar\rho_{k+\frac{1}{2}}, -\overline{M}^\xi_{k+\frac{1}{2}}, \overline{E}_{k+\frac{1}{2}}\right).$$

By the Dukowicz approximate Riemann solver, we obtain $u_v^1 = u_v^3 = 0$, $p^1 = p^3$ and u_v^2, u_v^4, p^2 and p^4 are independent of the 'l' index since $\mathbf{U}_v^{2\pm}$ and $\mathbf{U}_v^{4\pm}$ are independent of the 'l' index. The tangential velocities at each edge are as follows

$$u_t^1 = \frac{1}{2}\left(M_t^{1-}/\rho^{1-} + M_t^{1+}/\rho^{1+}\right) = \cos\left(\frac{1}{2}\Delta\varphi\right)\overline{M}^\xi_{k+\frac{1}{2}}/\bar\rho^\xi_{k+\frac{1}{2}},$$
$$u_t^3 = \frac{1}{2}\left(M_t^{3-}/\rho^{3-} + M_t^{3+}/\rho^{3+}\right) = \cos\left(\frac{1}{2}\Delta\varphi\right)\overline{M}^\xi_{k+\frac{1}{2}}/\bar\rho^\xi_{k+\frac{1}{2}},$$
$$u_t^2 = \frac{1}{2}\left(M_t^{2-}/\rho^{2-} + M_t^{2+}/\rho^{2+}\right) = 0,$$
$$u_t^4 = \frac{1}{4}\left(M_t^{4-}/\rho^{4-} + M_t^{4+}/\rho^{4+}\right) = 0.$$

By now, we can get the conclusion that the pressure, normal velocity and tangential velocity at the cell edges are symmetrical in the angular direction. For simplicity, we denote the pressure, normal velocity and tangential velocity at the edge connecting the points (k,l) and $(k,l+1)$ to be p_k, $(u_v)_k$ and $(u_t)_k$ for any $k \in [1,K]$, $l \in [1,L-1]$, and denote those at the edge connecting the points (k,l) and $(k+1,l)$ to be $p_{k+\frac{1}{2}}$, $(u_v)_{k+\frac{1}{2}}$ and $(u_t)_{k+\frac{1}{2}}$ for any $k \in [1,K-1]$, $l \in [1,L]$ respectively, namely, for Cell $I_{k+\frac{1}{2},l+\frac{1}{2}}$,

$$\begin{aligned} &p^1 = p^3 = p_{k+\frac{1}{2}}, \quad p^2 = p_{k+1}, \quad p^4 = p_k,\\ &u_v^1 = (u_v)_{k+\frac{1}{2}} = 0, \quad u_v^2 = (u_v)_{k+1}, \quad u_v^3 = -(u_v)_{k+\frac{1}{2}} = 0, \quad u_v^4 = -(u_v)_k,\\ &u_t^1 = u_t^3 = (u_t)_{k+\frac{1}{2}}, \quad u_t^2 = 0, \quad u_t^4 = 0. \end{aligned} \tag{2.18}$$

By now, we can conclude that the magnitude of the velocity at the cell edges in the radial direction with the same k index is identical and its direction is the edge's tangential direction. While the magnitude of the velocity at the cell edges in the angular direction with the same k index is identical and its direction is the edge's normal direction, see Fig. 2.2. All the values of the velocity are independent of the l index. Denote the value of the composite velocity at the edge connecting the points (k,l) and $(k,l+1)$ to be u_k for all $k \in [1,K]$, $l \in [1,L-1]$, and the value of the composite velocity at the edge connecting the points (k,l) and $(k+1,l)$ to be $u_{k+\frac{1}{2}}$ for $k \in [1,K-1]$, $l \in [1,L]$. Since the velocity at the vertex is obtained by the arithmetic average of the four velocities along its four connecting edges (see Section 2.2.2), we have, at the vertex (k,l) in Fig. 2.2,

$$\mathbf{u}_{k,l} = \frac{1}{4}\left(u_{k-\frac{1}{2}}\vec{A} + u_k\vec{B} + u_{k+\frac{1}{2}}\vec{C} + u_k\vec{D}\right) \tag{2.19}$$
$$= \frac{1}{4}\left(u_{k-\frac{1}{2}}\vec{A} + u_{k+\frac{1}{2}}\vec{C} + u_k(\vec{B}+\vec{D})\right), \tag{2.20}$$

where $\vec{A}$, $\vec{C}$ are the unit tangential vector and $\vec{B}$, $\vec{D}$ are the unit normal vector of the relative edges.

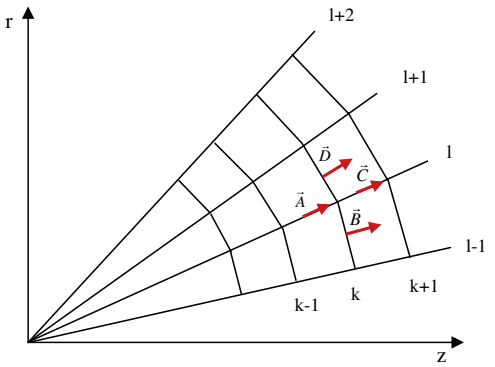

Fig. 2.2. The sketch of velocities at the edges connected to the vertex (k,l).

Since the grid is equi-angular, we have $\vec{A}=\vec{C},\ \vec{B}+\vec{D}=\alpha\vec{C}$, where $\alpha=2\cos\frac{1}{2}\Delta\varphi$ is a constant for the given equi-angular polar grids. Thus we get

$$\mathbf{u}_{k,l}=\frac{1}{4}\left(u_{k-\frac{1}{2}}+u_{k+\frac{1}{2}}+\alpha u_k\right)\vec{C}. \tag{2.21}$$

Eq. (2.21) indicates that the velocities at the vertices with the same k index are identical and their directions are along their radial directions. Thus we have finished the proof of the symmetry of the grid at the $(n+1)$th step.

Next we will prove that the symmetry can also be maintained for the evolved conserved variables at the $(n+1)$th step.

Using the symmetry property of grid at $(n+1)$th step, the area and volume of Cell $I_{k+\frac{1}{2},l+\frac{1}{2}}$ at the $(n+1)$th step can be denoted simply as follows

$$s^{n+1}_{k+\frac{1}{2},l+\frac{1}{2}}=s^{n+1}_{k+\frac{1}{2}},\quad V^{n+1}_{k+\frac{1}{2},l+\frac{1}{2}}=(r_c)^{n+1}_{k+\frac{1}{2},l+\frac{1}{2}}s^{n+1}_{k+\frac{1}{2}}=(\xi_c)^{n+1}_{k+\frac{1}{2}}\sin(\varphi_c)_{l+\frac{1}{2}}s^{n+1}_{k+\frac{1}{2}},$$

where r_c and ξ_c are the values of r and ξ at the cell center respectively. We have omitted the subscript '$l+\frac{1}{2}$' of those variables which are independent of the l index, and we have omitted the subscript '$k+\frac{1}{2}$' and superscript '$n+1$' of φ_c since they are independent of the k and n indices.

Thus, the term at the left hand of Eq. (2.14) can be rewritten as follows

$$\begin{pmatrix}\bar{\rho}^{n+1}_{k+\frac{1}{2},l+\frac{1}{2}}V^{n+1}_{k+\frac{1}{2},l+\frac{1}{2}}-\bar{\rho}^{n}_{k+\frac{1}{2},l+\frac{1}{2}}V^{n}_{k+\frac{1}{2},l+\frac{1}{2}}\\ \overline{M}^{\xi,n+1}_{k+\frac{1}{2},l+\frac{1}{2}}V^{n+1}_{k+\frac{1}{2},l+\frac{1}{2}}-\overline{M}^{\xi,n}_{k+\frac{1}{2},l+\frac{1}{2}}V^{n}_{k+\frac{1}{2},l+\frac{1}{2}}\\ \overline{M}^{\theta,n+1}_{k+\frac{1}{2},l+\frac{1}{2}}V^{n+1}_{k+\frac{1}{2},l+\frac{1}{2}}-\overline{M}^{\theta,n}_{k+\frac{1}{2},l+\frac{1}{2}}V^{n}_{k+\frac{1}{2},l+\frac{1}{2}}\\ \overline{E}^{n+1}_{k+\frac{1}{2},l+\frac{1}{2}}V^{n+1}_{k+\frac{1}{2},l+\frac{1}{2}}-\overline{E}^{n}_{k+\frac{1}{2},l+\frac{1}{2}}V^{n}_{k+\frac{1}{2},l+\frac{1}{2}}\end{pmatrix}=\sin(\varphi_c)_{l+\frac{1}{2}}\begin{pmatrix}\bar{\rho}^{n+1}_{k+\frac{1}{2},l+\frac{1}{2}}(\xi_c)^{n+1}_{k+\frac{1}{2}}s^{n+1}_{k+\frac{1}{2}}-\bar{\rho}_{k+\frac{1}{2}}(\xi_c)_{k+\frac{1}{2}}s_{k+\frac{1}{2}}\\ \overline{M}^{\xi,n+1}_{k+\frac{1}{2},l+\frac{1}{2}}(\xi_c)^{n+1}_{k+\frac{1}{2}}s^{n+1}_{k+\frac{1}{2}}-\overline{M}^{\xi}_{k+\frac{1}{2}}(\xi_c)_{k+\frac{1}{2}}s_{k+\frac{1}{2}}\\ \overline{M}^{\theta,n+1}_{k+\frac{1}{2},l+\frac{1}{2}}(\xi_c)^{n+1}_{k+\frac{1}{2}}s^{n+1}_{k+\frac{1}{2}}-\overline{M}^{\theta}_{k+\frac{1}{2}}(\xi_c)_{k+\frac{1}{2}}s_{k+\frac{1}{2}}\\ \overline{E}^{n+1}_{k+\frac{1}{2},l+\frac{1}{2}}(\xi_c)^{n+1}_{k+\frac{1}{2}}s^{n+1}_{k+\frac{1}{2}}-\overline{E}_{k+\frac{1}{2}}(\xi_c)_{k+\frac{1}{2}}s_{k+\frac{1}{2}}\end{pmatrix}. \tag{2.22}$$

The flux term in Eq. (2.14) can be expressed as follows

$$\begin{aligned}\sum_{m=1}^{M}\widehat{\mathbf{F}}(\mathbf{U}^m_v)\Delta l^m&=\begin{pmatrix}0\\ -p^1\sin\left(\frac{1}{2}\Delta\varphi\right)r^1_e\Delta l^1+p^2r^2_e\Delta l^2-p^3\sin\left(\frac{1}{2}\Delta\varphi\right)r^3_e\Delta l^3-p^4r^4_e\Delta l^4\\ -p^1\cos\left(\frac{1}{2}\Delta\varphi\right)r^1_e\Delta l^1+p^3\cos\left(\frac{1}{2}\Delta\varphi\right)r^3_e\Delta l^3\\ p^1u^1_vr^1_e\Delta l^1+p^2u^2_vr^2_e\Delta l^2+p^3u^3_vr^3_e\Delta l^3+p^4u^4_vr^4_e\Delta l^4\end{pmatrix}\\ &=\begin{pmatrix}0\\ -p^1\sin\left(\frac{1}{2}\Delta\varphi\right)\Delta l^1(r^1_e+r^3_e)+p^2r^2_e\Delta l^2-p^4r^4_e\Delta l^4\\ p^1\Delta l^1(r^3_e-r^1_e)\cos\left(\frac{1}{2}\Delta\varphi\right)\\ p^2u^2_vr^2_e\Delta l^2+p^4u^4_vr^4_e\Delta l^4\end{pmatrix},\end{aligned} \tag{2.23}$$

where $\mathbf{U}^{m,n}_v,\ \Delta l^{m,n}$ are simplified as $\mathbf{U}^m_v,\ \Delta l^m$.

Using (2.17), (2.18) and the following equalities

$$
\begin{aligned}
r_e^1 &= \xi_{k+\frac{1}{2}} \sin\left((\varphi_c)_{l+\frac{1}{2}} - \frac{1}{2}\Delta\varphi\right),\\
r_e^2 &= \xi_{k+1} \sin(\varphi_c)_{l+\frac{1}{2}},\\
r_e^3 &= \xi_{k+\frac{1}{2}} \sin\left((\varphi_c)_{l+\frac{1}{2}} + \frac{1}{2}\Delta\varphi\right),\\
r_e^4 &= \xi_k \sin(\varphi_c)_{l+\frac{1}{2}},
\end{aligned}
$$

we have

$$
\begin{aligned}
\sum_{m=1}^{M} \widehat{\mathbf{F}}(\mathbf{U}_v^m)\Delta l^m &= \begin{pmatrix} 0 \\ -p_{k+\frac{1}{2}}\xi_{k+\frac{1}{2}}\Delta l_{k+\frac{1}{2}} \sin(\Delta\varphi)\sin(\varphi_c)_{l+\frac{1}{2}} + p_{k+1}\xi_{k+1}\Delta l_{k+1}\sin(\varphi_c)_{l+\frac{1}{2}} - p_k\xi_k\Delta l_k \sin(\varphi_c)_{l+\frac{1}{2}} \\ p_{k+\frac{1}{2}}\Delta l_{k+\frac{1}{2}}\xi_{k+\frac{1}{2}} \sin(\Delta\varphi)\cos(\varphi_c)_{l+\frac{1}{2}} \\ p_{k+1}(u_v)_{k+1}\xi_{k+1}\Delta l_{k+1}\sin(\varphi_c)_{l+\frac{1}{2}} - p_k(u_v)_k\xi_k\Delta l_k \sin(\varphi_c)_{l+\frac{1}{2}} \end{pmatrix} \\
&= \begin{pmatrix} 0 \\ \sin(\varphi_c)_{l+\frac{1}{2}}(-p_{k+\frac{1}{2}}\xi_{k+\frac{1}{2}}\Delta l_{k+\frac{1}{2}}\sin(\Delta\varphi) + p_{k+1}\xi_{k+1}\Delta l_{k+1} - p_k\xi_k\Delta l_k) \\ p_{k+\frac{1}{2}}s_{k+\frac{1}{2}}\cos(\varphi_c)_{l+\frac{1}{2}} \\ \sin(\varphi_c)_{l+\frac{1}{2}}(p_{k+1}(u_v)_{k+1}\xi_{k+1}\Delta l_{k+1} - p_k(u_v)_k\xi_k\Delta l_k) \end{pmatrix}.
\end{aligned} \tag{2.24}
$$

Using the equality (2.13), the source term in Eq. (2.14) takes the following form

$$
\begin{pmatrix} 0 \\ (p_c)^n_{k+\frac{1}{2},l+\frac{1}{2}}\sin(\varphi_c)^n_{k+\frac{1}{2},l+\frac{1}{2}}s^n_{k+\frac{1}{2},l+\frac{1}{2}} \\ (p_c)^n_{k+\frac{1}{2},l+\frac{1}{2}}\cos(\varphi_c)^n_{k+\frac{1}{2},l+\frac{1}{2}}s^n_{k+\frac{1}{2},l+\frac{1}{2}} \\ 0 \end{pmatrix} = \begin{pmatrix} 0 \\ p_{k+\frac{1}{2}}s_{k+\frac{1}{2}}\sin(\varphi_c)_{l+\frac{1}{2}} \\ p_{k+\frac{1}{2}}s_{k+\frac{1}{2}}\cos(\varphi_c)_{l+\frac{1}{2}} \\ 0 \end{pmatrix}.
$$

Thus the scheme (2.14) can be written as

$$
\begin{aligned}
&\sin(\varphi_c)_{l+\frac{1}{2}} \begin{pmatrix} \bar{\rho}^{n+1}_{k+\frac{1}{2},l+\frac{1}{2}}(\xi_c)^{n+1}_{k+\frac{1}{2}}s^{n+1}_{k+\frac{1}{2}} - \bar{\rho}_{k+\frac{1}{2}}(\xi_c)_{k+\frac{1}{2}}s_{k+\frac{1}{2}} \\ \overline{M}^{\xi,n+1}_{k+\frac{1}{2},l+\frac{1}{2}}(\xi_c)^{n+1}_{k+\frac{1}{2}}s^{n+1}_{k+\frac{1}{2}} - \overline{M}^{\xi}_{k+\frac{1}{2}}(\xi_c)_{k+\frac{1}{2}}s_{k+\frac{1}{2}} \\ \overline{M}^{\theta,n+1}_{k+\frac{1}{2},l+\frac{1}{2}}(\xi_c)^{n+1}_{k+\frac{1}{2}}s^{n+1}_{k+\frac{1}{2}} - \overline{M}^{\theta}_{k+\frac{1}{2}}(\xi_c)_{k+\frac{1}{2}}s_{k+\frac{1}{2}} \\ \overline{E}^{n+1}_{k+\frac{1}{2},l+\frac{1}{2}}(\xi_c)^{n+1}_{k+\frac{1}{2}}s^{n+1}_{k+\frac{1}{2}} - \overline{E}_{k+\frac{1}{2}}(\xi_c)_{k+\frac{1}{2}}s_{k+\frac{1}{2}} \end{pmatrix} \\
&= \Delta t\left(-\begin{pmatrix} 0 \\ \sin(\varphi_c)_{l+\frac{1}{2}}(-p_{k+\frac{1}{2}}\xi_{k+\frac{1}{2}}\Delta l_{k+\frac{1}{2}}\sin(\Delta\varphi) + p_{k+1}\xi_{k+1}\Delta l_{k+1} - p_k\xi_k\Delta l_k) \\ p_{k+\frac{1}{2}}s_{k+\frac{1}{2}}\cos(\varphi_c)_{l+\frac{1}{2}} \\ \sin(\varphi_c)_{l+\frac{1}{2}}(p_{k+1}(u_v)_{k+1}\xi_{k+1}\Delta l_{k+1} - p_k(u_v)_k\xi_k\Delta l_k) \end{pmatrix} + \begin{pmatrix} 0 \\ p_{k+\frac{1}{2}}s_{k+\frac{1}{2}}\sin(\varphi_c)_{l+\frac{1}{2}} \\ p_{k+\frac{1}{2}}s_{k+\frac{1}{2}}\cos(\varphi_c)_{l+\frac{1}{2}} \\ 0 \end{pmatrix}\right) \\
&= \Delta t\sin(\varphi_c)_{l+\frac{1}{2}} \begin{pmatrix} 0 \\ p_{k+\frac{1}{2}}\xi_{k+\frac{1}{2}}\Delta l_{k+\frac{1}{2}}\sin(\Delta\varphi) - p_{k+1}\xi_{k+1}\Delta l_{k+1} + p_k\xi_k\Delta l_k + p_{k+\frac{1}{2}}s_{k+\frac{1}{2}} \\ 0 \\ -p_{k+1}(u_v)_{k+1}\xi_{k+1}\Delta l_{k+1} + p_k(u_v)_k\xi_k\Delta l_k \end{pmatrix},
\end{aligned} \tag{2.25}
$$

$$
\begin{pmatrix} \bar{\rho}^{n+1}_{k+\frac{1}{2},l+\frac{1}{2}} \\ \overline{M}^{\xi,n+1}_{k+\frac{1}{2},l+\frac{1}{2}} \\ \overline{M}^{\theta,n+1}_{k+\frac{1}{2},l+\frac{1}{2}} \\ \overline{E}^{n+1}_{k+\frac{1}{2},l+\frac{1}{2}} \end{pmatrix} = \frac{1}{(\xi_c)^{n+1}_{k+\frac{1}{2}}s^{n+1}_{k+\frac{1}{2}}}\left(\begin{pmatrix} \bar{\rho}_{k+\frac{1}{2}}(\xi_c)_{k+\frac{1}{2}}s_{k+\frac{1}{2}} \\ \overline{M}^{\xi}_{k+\frac{1}{2}}(\xi_c)_{k+\frac{1}{2}}s_{k+\frac{1}{2}} \\ 0 \\ \overline{E}_{k+\frac{1}{2}}(\xi_c)_{k+\frac{1}{2}}s_{k+\frac{1}{2}} \end{pmatrix} + \Delta t\begin{pmatrix} 0 \\ p_{k+\frac{1}{2}}\xi_{k+\frac{1}{2}}\Delta l_{k+\frac{1}{2}}\sin(\Delta\varphi) - p_{k+1}\xi_{k+1}\Delta l_{k+1} + p_k\xi_k\Delta l_k + p_{k+\frac{1}{2}}s_{k+\frac{1}{2}} \\ 0 \\ -p_{k+1}(u_v)_{k+1}\xi_{k+1}\Delta l_{k+1} + p_k(u_v)_k\xi_k\Delta l_k \end{pmatrix}\right). \tag{2.26}
$$

By now, we can make the conclusion that $\left(\bar{\rho}^{n+1}_{k+\frac{1}{2},l+\frac{1}{2}}, \overline{M}^{\xi,n+1}_{k+\frac{1}{2},l+\frac{1}{2}}, \overline{M}^{\theta,n+1}_{k+\frac{1}{2},l+\frac{1}{2}}, \overline{E}^{n+1}_{k+\frac{1}{2},l+\frac{1}{2}}\right)$ only depend on the k index and are independent of the l index. Thus we have proved the symmetry preservation property of the scheme.

Remark. In practice, we can also implement the scheme in the z–r coordinates directly which has the following form with the Euler forward time discretization

$$\begin{pmatrix} \bar{\rho}^{n+1}_{k+\frac{1}{2},l+\frac{1}{2}} V^{n+1}_{k+\frac{1}{2},l+\frac{1}{2}} - \bar{\rho}^{n}_{k+\frac{1}{2},l+\frac{1}{2}} V^{n}_{k+\frac{1}{2},l+\frac{1}{2}} \\ \overline{M}^{z,n+1}_{k+\frac{1}{2},l+\frac{1}{2}} V^{n+1}_{k+\frac{1}{2},l+\frac{1}{2}} - \overline{M}^{z,n}_{k+\frac{1}{2},l+\frac{1}{2}} V^{n}_{k+\frac{1}{2},l+\frac{1}{2}} \\ \overline{M}^{r,n+1}_{k+\frac{1}{2},l+\frac{1}{2}} V^{n+1}_{k+\frac{1}{2},l+\frac{1}{2}} - \overline{M}^{r,n}_{k+\frac{1}{2},l+\frac{1}{2}} V^{n}_{k+\frac{1}{2},l+\frac{1}{2}} \\ \overline{E}^{n+1}_{k+\frac{1}{2},l+\frac{1}{2}} V^{n+1}_{k+\frac{1}{2},l+\frac{1}{2}} - \overline{E}^{n}_{k+\frac{1}{2},l+\frac{1}{2}} V^{n}_{k+\frac{1}{2},l+\frac{1}{2}} \end{pmatrix} = \Delta t^n \left(-\sum_{m=1}^{M} \widehat{\mathbf{F}}(\mathbf{U}_v^{m,n}) \Delta l^{m,n} + \begin{pmatrix} 0 \\ 0 \\ (p_c)^n_{k+\frac{1}{2},l+\frac{1}{2}} S^n_{k+\frac{1}{2},l+\frac{1}{2}} \\ 0 \end{pmatrix} \right), \tag{2.27}$$

where

$$\overline{M}^z_{k+\frac{1}{2},l+\frac{1}{2}} = \frac{1}{V_{k+\frac{1}{2},l+\frac{1}{2}}} \iint_{I_{k+\frac{1}{2},l+\frac{1}{2}}} M_z r \, dr \, dz,$$

$$\overline{M}^r_{k+\frac{1}{2},l+\frac{1}{2}} = \frac{1}{V_{k+\frac{1}{2},l+\frac{1}{2}}} \iint_{I_{k+\frac{1}{2},l+\frac{1}{2}}} M_r r \, dr \, dz,$$

$$\widehat{\mathbf{F}} = \begin{pmatrix} \hat{f}_D(\mathbf{U}_v^-, \mathbf{U}_v^+) \\ \hat{f}_{M^z}(\mathbf{U}_v^-, \mathbf{U}_v^+) \\ \hat{f}_{M^r}(\mathbf{U}_v^-, \mathbf{U}_v^+) \\ \hat{f}_E(\mathbf{U}_v^-, \mathbf{U}_v^+) \end{pmatrix}$$

and

$$\begin{cases} \hat{f}_D(\mathbf{U}_v, \mathbf{U}_v) = 0, \\ \hat{f}_{M^z}(\mathbf{U}_v, \mathbf{U}_v) = p n_z r, \\ \hat{f}_{M^r}(\mathbf{U}_v, \mathbf{U}_v) = p n_r r, \\ \hat{f}_E(\mathbf{U}_v, \mathbf{U}_v) = p u_v r, \end{cases}$$

$\hat{f}_D$, $\hat{f}_{M^z}$, $\hat{f}_{M^r}$ and $\hat{f}_E$ are the numerical fluxes for mass, z-momentum, r-momentum and total energy across the cell boundary respectively. Similar procedures described in this section are used to determine these numerical fluxes and the vertex velocity. $(p_c)^n_{k+\frac{1}{2},l+\frac{1}{2}}$ in the source term is determined by the formula (2.13).

3. Numerical results in the two-dimensional cylindrical coordinates

In this section, we perform numerical experiments in two-dimensional cylindrical coordinates. Purely Lagrangian computation, second-order Runge–Kutta time discretization and the ideal gas with $\gamma = 5/3$ are used in the following tests unless otherwise stated. Reflective boundary conditions are applied to the z and r axes in all the tests.

3.1. Accuracy test

We test the accuracy of our scheme on a free expansion problem given in [23]. The initial computational domain is $[0,1] \times [0,\pi/2]$ defined in the polar coordinates. The gas is initially at rest with uniform density $\rho = 1$ and pressure has the following distribution

$$p = 1 - (z^2 + r^2).$$

The analytical solution of the problem is as follows

$$R(t) = \sqrt{1 + 2t^2},$$

$$u_\xi(z,r,t) = \frac{2t}{1+2t^2}\sqrt{z^2+r^2},$$

$$\rho(z,r,t) = \frac{1}{R^3},$$

$$p(z,r,t) = \frac{1}{R^5}\left(1 - \frac{z^2+r^2}{R^2}\right),$$

where R is the radius of the free outer boundary and u_ξ represents the value of velocity in the radial direction.

Table 3.1
Errors of the scheme in 2D cylindrical coordinates for the free expansion problem using $K \times L$ initially equi-angular polar grid cells.

$K = L$	Norm	Density	Order	Momentum	Order	Energy	Order
20	L_1	0.20E−2		0.42E−2		0.12E−2	
	L_∞	0.52E−2		0.71E−2		0.45E−2	
40	L_1	0.11E−2	0.86	0.21E−2	0.95	0.60E−3	1.05
	L_∞	0.28E−2	0.90	0.39E−2	0.86	0.24E−2	0.88
80	L_1	0.57E−3	0.94	0.11E−2	0.96	0.31E−3	0.95
	L_∞	0.15E−2	0.92	0.21E−2	0.87	0.13E−2	0.93
160	L_1	0.30E−3	0.92	0.57E−3	0.95	0.17E−3	0.88
	L_∞	0.75E−3	0.98	0.12E−2	0.85	0.65E−3	0.98

Free boundary condition is applied on the outer boundary. The errors of the scheme at $t = 1$ are listed in Table 3.1 which are measured on the interval $[\frac{1}{5}K, \frac{4}{5}K] \times [1, L]$ to remove the influence from the boundary. In Table 3.1, we can see the expected first order accuracy for all the evolved conserved variables.

3.2. Non-oscillatory tests

Example 1 (*The Noh problem in a cylindrical coordinate system [21]*). We test the Noh problem which is a well known test problem widely used to validate Lagrangian scheme in the regime of strong shock waves. In this test case, the initial state of the fluid is uniform with $(\rho, e) = (1, 10^{-5})$ and an inward radial velocity of magnitude 1. The equi-angular polar grid is applied in the $\frac{1}{4}$-circle computational domain defined in the polar coordinates by $[0,1] \times [0, \pi/2]$. The shock is generated in a perfect gas by bringing the cold gas to rest at the origin. The analytical post shock density is 64 and the shock speed is 1/3. Fig. 3.1 shows the initial grid and the final grid at $t = 0.6$ with 200×20 cells and density as a function of radial radius at $t = 0.6$ for two different angular zonings ($200 \times 20, 200 \times 40$). In the plot of the grid, we observe the symmetry is perfectly preserved. In the plot of density, we observe no spurious oscillation near the discontinuity region. The shock location and the shock magnitude are closer to the analytical solution with the refinement of the grid in the angular direction which reflects the convergence trend of the numerical solution toward the analytical solution.

Example 2 (*The one-dimensional spherical Sod problem*). The Riemann problem proposed by Sod is tested in the cylindrical coordinates. The initial computational domain is a $\frac{1}{4}$-circle region defined in the polar coordinates by $[0, 20] \times [0, \pi/2]$. Its initial condition is as follows

$$(\rho, u_\xi, p) = (1.0, 0, 1.0), \quad 0 \leqslant \xi \leqslant 10,$$
$$(\rho, u_\xi, p) = (0.125, 0, 0.1), \quad 10 < \xi \leqslant 20.$$

Reflective boundary condition is applied on the outer boundary. The reference solution is the converged result obtained by using a one-dimensional second-order Eulerian code in the spherical coordinate with 10,000 grid points. We display in Fig. 3.2 the numerical results of the grid and density as a function of the radial radius and the surface of density performed by our scheme with 400×10 equi-angular polar cells at $t = 1.4$. We observe the symmetrical behavior of our scheme and good agreement between our numerical result and the reference solution.

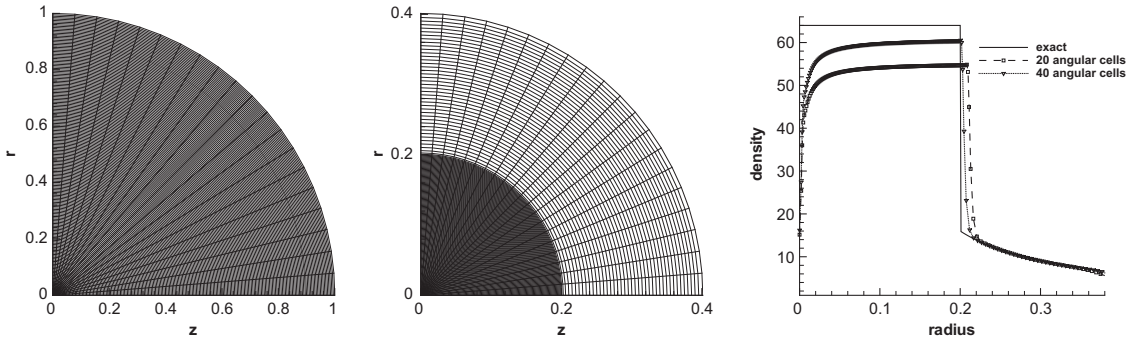

Fig. 3.1. The result of the Noh problem at $t = 0.6$. Left: initial grid with 200×20 cells; Middle: final grid with 200×20 cells; Right: density vs radial radius with 200×20 and 200×40 cells respectively. Solid line: exact solution; dashed line: computational solution.

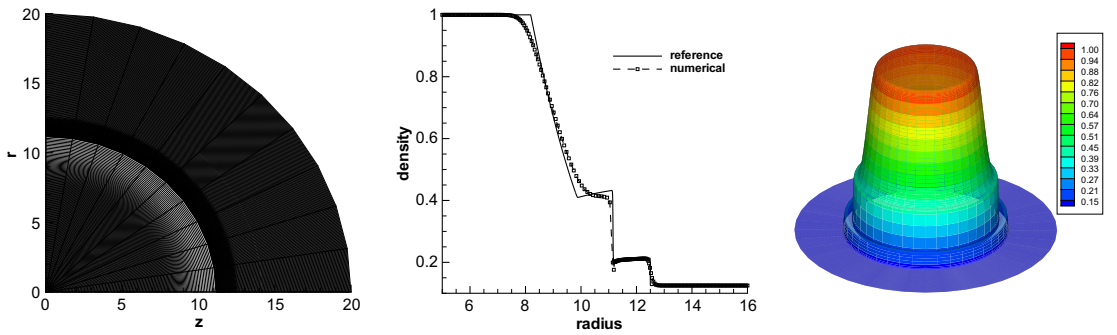

Fig. 3.2. The result of the Sod problem at $t = 1.4$. Left: final grid with 400×10 cells; Middle: density versus radial radius. Solid line: exact solution; dashed line: computational solution; Right: surface of density in the whole circle region obtained by a mirror image.

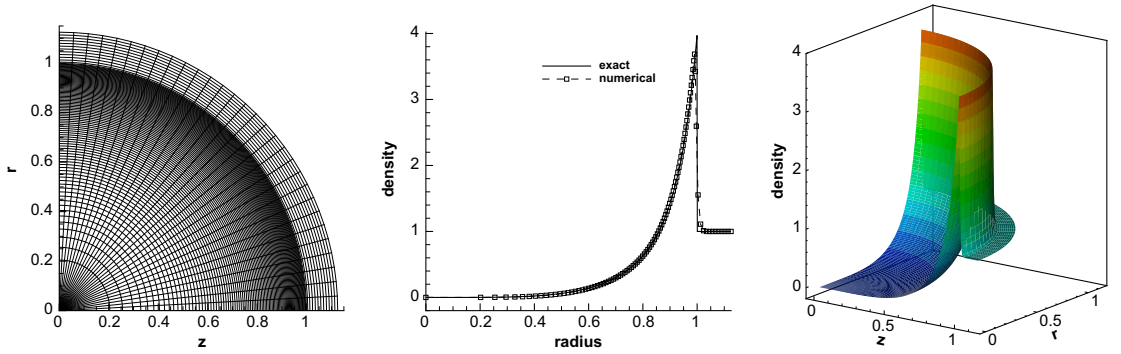

Fig. 3.3. The result of the Sedov problem with 100×30 cells at $t = 1.0$. Left: final grid; Middle: density versus radial radius. Solid line: exact solution; dashed line: computational solution; Right: surface of density.

Example 3 (*The Sedov problem in a cylindrical coordinate system [23]*). We present the result of the Sedov blast wave in a cylindrical coordinate system as an example of a diverging shock wave. The initial computational domain is a $\frac{1}{4}$-circle region defined in the polar coordinates by $[0, 1.125] \times [0, \pi/2]$ consisting of 100×30 equi-angular polar grids. The initial density is unity and the initial velocity is zero. The internal energy is zero except in the cells connecting the origin where they share a total value of 0.2468. Reflective boundary condition is applied on the outer boundary. The analytical solution is a shock at radius unity at time unity with a peak density of 4. The final grid, density as a function of the radial radius and surface of density are displayed in Fig. 3.3. We observe the expected symmetry in the plot of grid. The position of shock and peak density are in quite satisfactory agreement with the analytical solution without any spurious oscillations which demonstrates the good performance of the scheme in symmetrical, non-oscillatory and accuracy properties.

Example 4 (*Implosion problem of Lazarus [15]*). The implosion problem of Lazarus is a problem with self-similar solution. A sphere of unit initial radius with zero specific internal energy and unit density is driven by an inward radial velocity given by

$$u_\xi(t) = \frac{-\alpha f}{(1 - ft)^{1-\alpha}} \tag{3.1}$$

where $\alpha = 0.6883545$, $f = 1 - \varepsilon t - \delta t^3$, $\varepsilon = 0.185$, $\delta = 0.28$.

We use a grid of 200×30 equal-angle polar cells in the initial computational domain $[0, 1] \times [0, \pi/2]$ defined in the polar coordinates. The numerically converged result computed using a one-dimensional second-order Lagrangian code in the spherical coordinate with 10,000 cells is used as a reference solution. Here the Courant number initially is taken as a smaller value at 0.1, and after $t = 0.01$ it returns to the normal value 0.5. Fig. 3.4 shows the results of the grid and surface of density using 200×30 grids at $t = 0.8$ and density as a radial radius function at the typical time $t = 0.74, 0.8$ with two different angular zoned grids ($200 \times 30, 200 \times 60$) respectively. In the plot of the grid, we notice that symmetry is preserved quite well as expected for the scheme. In the plot of density, the non-oscillatory and accurate numerical solution and the convergence tendency of the numerical results toward the reference solution are observed.

Example 5 (*Kidder's isentropic compression problem [14,17]*). This problem involves a self-similar isentropic compression of a shell filled with perfect gas which is usually used to validate the ability of a Lagrangian scheme in computing a spherical isentropic compression. The shell initially is a ring shaped region with the internal radius ξ_1 and the external radius ξ_2. The initial density and pressure ρ_0, p_0 are defined as follows

$$\rho_0(\xi) = \left(\frac{\xi_2^2 - \xi^2}{\xi_2^2 - \xi_1^2}\rho_1^{\gamma-1} + \frac{\xi^2 - \xi_1^2}{\xi_2^2 - \xi_1^2}\rho_2^{\gamma-1}\right)^{\frac{1}{\gamma-1}}, \quad p_0(\xi) = s(\rho_0(\xi))^{\gamma},$$

where $\xi_1 = 0.9$, $\xi_2 = 1.0$, $\rho_1 = 6.31 \times 10^{-4}$, $\rho_2 = 10^{-2}$, $s = 2.15 \times 10^4$, $\gamma = 5/3$. The pressure $p_1(t)$ and $p_2(t)$ are imposed continuously at the internal and external boundary of the shell respectively which have the following representation

$$p_1(t) = p_1^0 a(t)^{-\frac{2\gamma}{\gamma-1}}, \quad p_2(t) = p_2^0 a(t)^{-\frac{2\gamma}{\gamma-1}},$$

where $p_1^0 = 0.1$, $p_2^0 = 10$ and $a(t) = \sqrt{1 - \left(\frac{t}{\tau}\right)^2}$ in which $\tau = 6.72 \times 10^{-3}$ is the focusing time of the shell and $t \in [0, \tau)$ is the evolving time.

Denote $\zeta(\xi, t)$ to be the radius at the time t of a point initially located at radius ξ, its analytical solution is $\zeta(\xi, t) = a(t)\xi$. The analytical solutions of three fundamental variables for this problem in spherical geometry are as follows

$$\rho(\zeta(\xi,t),t) = \rho_0(\xi)\xi a(t)^{-\frac{2}{\gamma-1}},$$
$$u(\zeta(\xi,t),t) = \xi\frac{d}{dt}a(t),$$
$$p(\zeta(\xi,t),t) = p_0(\xi)\xi a(t)^{-\frac{2\gamma}{\gamma-1}}.$$

We test the problem initially on the computational region $[0.9, 1] \times [0, \pi/2]$ in the polar coordinates with 40×20, 80×40, 160×80 grids respectively. The final time is set to be $t = 0.99\tau$. Fig. 3.5 shows the initial and final grids and the time evolution of the position of the external boundary with 40×20 grids. Fig. 3.6 shows the results of density, velocity and pressure at the final time. From these figures, we can see the perfect symmetry in the grid. The trajectory of the external boundary coincides with the analytical solution quite well. The numerical solutions of density, velocity and pressure converge to the analytical solutions asymptotically.

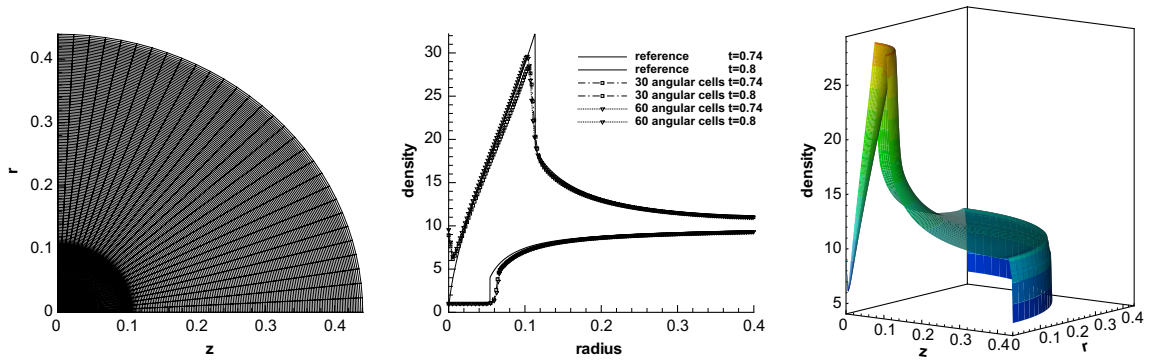

Fig. 3.4. The result of the Lazarus problem. Left: final grid with 200×30 cells at $t = 0.8$; Middle: density versus radial radius at $t = 0.74$, *0.8* with 200×30 and 200×60 cells respectively. Solid line: reference solution; dashed line: computational solution; Right: surface of density at $t = 0.8$ with 200×30 cells.

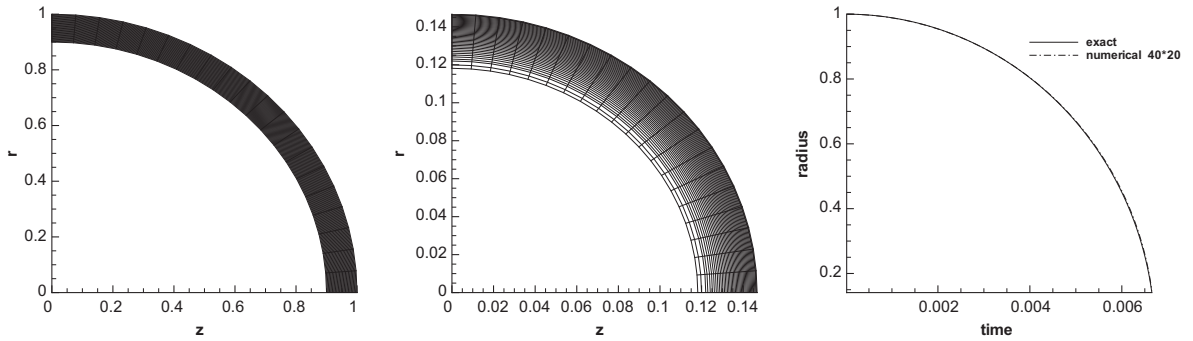

Fig. 3.5. The result of the Kidder problem with 40×20 grids. Left: initial grid; Middle: final grid at $t = 0.99\tau$; Right: trajectory of external boundary compared with the exact solution. Solid line: exact solution; dashed line: computational solution.

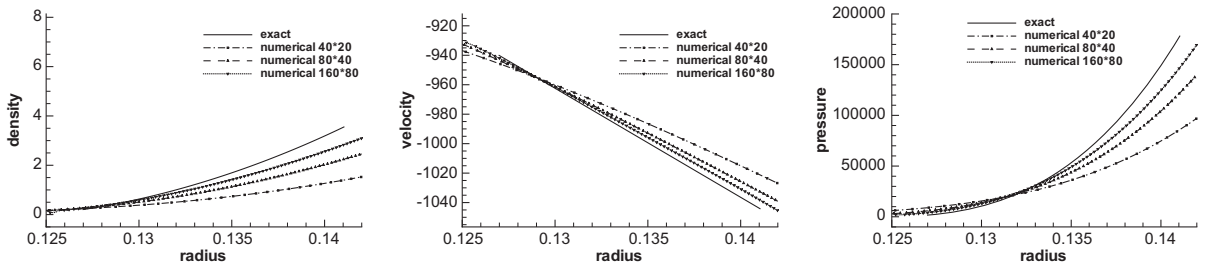

Fig. 3.6. The result of the Kidder problem at $t = 0.99\tau$ with three different zonings. Left: density versus radial radius; Middle: velocity vs radial radius; Right: pressure vs radial radius. Solid line: exact solution; dashed line: computational solution.

Example 6 (*Coggeshall expansion problem [10]*). This is a two-dimensional adiabatic compression problem proposed by Coggeshall. The computational domain consists of a quarter of a sphere of unit radius zoned with 100×10 grids. The initial density is unity and the initial velocity at the grid vertices is given as $(u_z, u_r) = (-z/4, -r)$. The specific internal energy of a cell is given as $e = (3z_c/8)^2$, where z_c is the z coordinate of the cell center. Fig. 3.7 shows the results of the grid and density plotted as a function of the radial radius along each l line at the time of 0.8 when the analytical density is expected to be flat with a value of 37.4. From the figures, we can observe the numerical result is in agreement with the analytical solution except for the small region near the origin. This example serves the purpose of testing the performance of our scheme on a problem with an initial equal-angle-zoned grid evolving into a non-symmetric grid.

Example 7 (*Cylindrical Noh problem on the Cartesian grid [21]*). We test the Noh problem with the Cartesian grid in a cylindrical coordinate system to verify the performance of our scheme on non-polar grid. The problem domain is $[0,1] \times [0,1]$. The initial state of the fluid is uniform with $(\rho, u_z, u_r, e) = (1, 0, -1, 10^{-5})$. Reflective boundary conditions are applied on the left, right and lower boundaries. Inflow boundary condition is used on the upper boundary. The shock is generated in a perfect gas by bringing the cold gas to rest at a rigid wall ($r = 0$). The analytical post shock density is 16 and the shock speed is 1/3. Fig. 3.8 shows the Lagrangian simulation results of our schemes at $t = 0.6$ with 10×200 grids. We observe good performance of our scheme in this problem on the Cartesian quadrilateral grid.

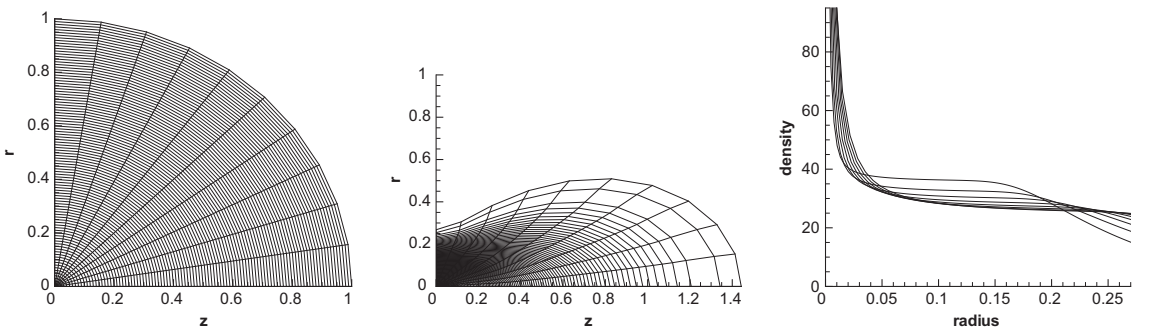

Fig. 3.7. The result of the Coggeshall problem at $t = 0.8$. Left: initial grid; Middle: final grid; Right: density versus the radial radius.

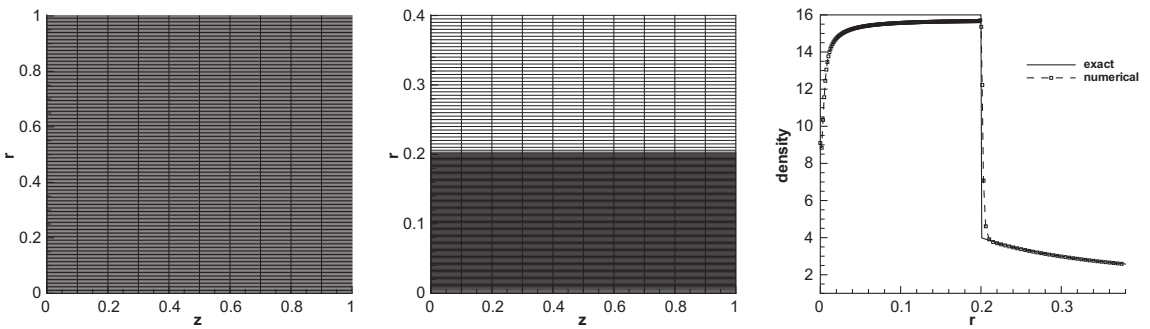

Fig. 3.8. The result of the Noh problem at $t = 0.6$. Left: initial grid; Middle: final grid; Right: density as a function of r. Solid line: exact solution; dashed line: computational solution.

4. Concluding remarks

In this paper we have described a new cell-centered Lagrangian schemes for solving Euler equations in cylindrical coordinates. The scheme can preserve the symmetry property for one-dimensional spherical problem computed on an equal-angle-zoned initial grid. Compared with many current Lagrangian type schemes, our scheme has the distinguished feature in being able to guarantee both symmetry and conservation properties for all conserved variables including mass, momentum and total energy. Several two-dimensional examples in the cylindrical coordinates have been presented which demonstrate the good performance of the scheme. The strategy proposed in this paper is hopefully applicable to certain other existing schemes to obtain the symmetry property without loss of their original good properties. This generalization, as well as the improvement of the scheme in accuracy and robustness, constitute our future work.

References

[1] D.J. Benson, Momentum advection on a staggered mesh, Journal of Computational Physics 100 (1992) 143–162.
[2] D.J. Benson, Computational methods in Lagrangian and Eulerian hydrocodes, Computer Methods in Applied Mechanics and Engineering 99 (1992) 235–394.
[3] P.L. Browne, Integrated gradients: a derivation of some difference forms for the equation of motion for compressible flow in two-dimensional Lagrangian hydrodynamics, using integration of pressures over surfaces, Los Alamos National Laboratory Report LA-2105872-MS, 1986.
[4] E.J. Caramana, D.E. Burton, M.J. Shashkov, P.P. Whalen, The construction of compatible hydrodynamics algorithms utilizing conservation of total energy, Journal of Computational Physics 146 (1998) 227–262.
[5] E.J. Caramana, P.P. Whalen, Numerical preservation of symmetry properties of continuum problems, Journal of Computational Physics 141 (1998) 174–198.
[6] E.J. Caramana, M.J. Shashkov, P.P. Whalen, Formulations of artificial viscosity for multidimensional shock wave computations, Journal of Computational Physics 144 (1998) 70–97.
[7] J.C. Campbell, M.J. Shashkov, A tensor artificial viscosity using a mimetic finite difference algorithm, Journal of Computational Physics 172 (2001) 739–765.
[8] J. Cheng, C.-W. Shu, A high order ENO conservative Lagrangian type scheme for the compressible Euler equations, Journal of Computational Physics 227 (2007) 1567–1596.
[9] J. Cheng, C.-W. Shu, A third order conservative Lagrangian type scheme on curvilinear meshes for the compressible Euler equation, Communications in Computational Physics 4 (2008) 1008–1024.
[10] S.V. Coggeshall, J. Meyer-ter-Vehn, Group invariant solutions and optimal systems for multidimensional hydrodynamics, Journal of Mathematical Physics 33 (1992) 3585–3601.
[11] B. Després, C. Mazeran, Lagrangian gas dynamics in two dimensions and lagrangian systems, Archive for Rational Mechanics and Analysis 178 (2005) 327–372.
[12] J.K. Dukowicz, A general, non-iterative Riemann solver for Godunov method, Journal of Computational Physics 61 (1985) 119–137.
[13] C. Hirt, A. Amsden, J. Cook, An arbitrary Lagrangian–Eulerian computing method for all flow speeds, Journal of Computational Physics 14 (1974) 227–253.
[14] R.E. Kidder, Laser-driven compression of hollow shells: power requirements and stability limitations, Nuclear Fusion 1 (1976) 3–14.
[15] R. Lazarus, Self-similar solutions for converging shocks and collapsing cavities, SIAM Journal on Numerical Analysis 18 (1981) 316–371.
[16] P.-H. Maire, R. Abgrall, J. Breil, J. Ovadia, A cell-centered Lagrangian scheme for compressible flow problems, SIAM Journal of Scientific Computing 29 (2007) 1781–1824.
[17] P.-H. Maire, A high-order cell-centered Lagrangian scheme for compressible fluid flows in two-dimensional cylindrical geometry, Journal of Computational Physics 228 (2009) 6882–6915.
[18] L.G. Margolin, M.J. Shashkov, Using a curvilinear grid to construct symmetry-preserving discretizations for Lagrangian gas dynamics, Journal of Computational Physics 149 (1999) 389–417.
[19] C.D. Munz, On Godunov-type schemes for Lagrangian gas dynamics, SIAM Journal on Numerical Analysis 31 (1994) 17–42.
[20] J. von Neumann, R.D. Richtmyer, A method for the calculation of hydrodynamics shocks, Journal of Applied Physics 21 (1950) 232–237.
[21] W.F. Noh, Errors for calculations of strong shocks using an artificial viscosity and an artificial heat flux, Journal of Computational Physics 72 (1987) 78–120.
[22] W.D. Schulz, Two-dimensional Lagrangian hydrodynamic difference equations, Methods of Computational Physics 3 (1964) 1–45.
[23] L.I. Sedov, Similarity and Dimensional Methods in Mechanics, Academic Press, New York, 1959.
[24] C.-W. Shu, S. Osher, Efficient implementation of essentially non-oscillatory shock-capturing schemes, Journal of Computational Physics 77 (1988) 439–471.
[25] A. Solov'ev, M. Shashkov, Difference scheme for the Dirichlet particle method in cylindrical coordinates, conserving symmetry of gas-dynamical flow, Differential Equations 24 (1988) 817–823.
[26] M.L. Wilkins, Calculation of elastic plastic flow, Methods of Computational Physics 3 (1964) 211–263.
[27] Z. Xu, C.-W. Shu, Anti-diffusive flux corrections for high order finite difference WENO schemes, Journal of Computational Physics 205 (2005) 458–485.